Journal of Neuroscience Methods 256 (2015) 9–21

Contents lists available at ScienceDirect

Journal of Neuroscience Methods

journal homepage: www.elsevier.com/locate/jneumeth

Clinical Neuroscience

EEG source localization: Sensor density and head surface coverage

Jasmine Song[a,*,1], Colin Davey[a,1], Catherine Poulsen[a,1], Phan Luu[a,b,1], Sergei Turovets[a,c,1], Erik Anderson[a,1], Kai Li[a,1], Don Tucker[a,b,1]

[a] Electrical Geodesics, Inc., Eugene, OR, USA
[b] Department of Psychology, University of Oregon, Eugene, OR, USA
[c] Neuroinformatics Center, University of Oregon, Eugene, OR, USA

HIGHLIGHTS

- Sensors on inferior surface improve localization accuracy for deep sources.
- Sensors on inferior surface reduce error variability of sources at all depths.
- Sensors on inferior surface improve localization accuracy even with sparse arrays.
- Most accurate source localization is obtained with whole-head, dense-array sampling.

ARTICLE INFO

Article history:
Received 6 July 2015
Received in revised form 10 August 2015
Accepted 12 August 2015
Available online 20 August 2015

Keywords:
Dense array EEG
Source localization
Minimum norm
SLORETA
FDM
Epilepsy

ABSTRACT

Background: The accuracy of EEG source localization depends on a sufficient sampling of the surface potential field, an accurate conducting volume estimation (head model), and a suitable and well-understood inverse technique. The goal of the present study is to examine the effect of sampling density and coverage on the ability to accurately localize sources, using common linear inverse weight techniques, at different depths. Several inverse methods are examined, using the popular head conductivity.
New method: Simulation studies were employed to examine the effect of spatial sampling of the potential field at the head surface, in terms of sensor density and coverage of the inferior and superior head regions. In addition, the effects of sensor density and coverage are investigated in the source localization of epileptiform EEG.
Results: Greater sensor density improves source localization accuracy. Moreover, across all sampling density and inverse methods, adding samples on the inferior surface improves the accuracy of source estimates at all depths.
Comparison with existing methods: More accurate source localization of EEG data can be achieved with high spatial sampling of the head surface electrodes.
Conclusions: The most accurate source localization is obtained when the voltage surface is densely sampled over both the superior and inferior surfaces.

1. Introduction

The electroencephalogram (EEG) recorded at the head surface provides important information on brain activity in both clinical applications (Michel et al., 2004; Lantz et al., 2003; Holmes, 2008; Brodbeck et al., 2011) and neuroscience research (Brunet et al., 2011; Dale and Sereno, 1993; Delorme et al., 2007; Hassan et al., 2014). Traditionally the EEG was recorded only at a few scalp locations measured by the percentages between skull landmarks with the International Ten-Twenty System (Jasper, 1958). The EEG reflects not only the neural activity of the cortex but also various sources of noise (including non-cephalic biological, environmental, and instrument noise).

Although it is the head surface potentials that are measured, researchers and clinicians ultimately want to discern the cortical sources of relevant EEG features. The dipolar fields of each brain region propagate in three dimensions, in a dipolar pattern depending on the orientation of the cortical sources. Activity recorded at any head surface sensor reflects a summation of all active sources in the brain, superposed as a function of their distance, orientation,

* Corresponding author at: 500 East 4th Avenue, Ste 200, Eugene, OR 97401, USA. Tel.: +1 541 687 7962; fax: +1 541 687 7963.
E-mail address: jsong@egi.com (J. Song).
[1] The authors are employees of EGI, a manufacturer of dense array EEG systems.

http://dx.doi.org/10.1016/j.jneumeth.2015.08.015

and the resistivity of the underlying tissues. Therefore, realistic source analysis of EEG potentials requires objective biophysical models that incorporate the exact positions of the sensors as well as the properties of head and brain anatomy, such that appropriate inverse techniques can be applied to map surface potentials to cortical sources (Michel et al., 2004).

In biophysical models, current sources in the brain are typically modeled using dipoles that are assumed to be equivalent to the summated post-synaptic potentials of all the aligned pyramidal cells in a patch of cerebral cortex. The cortex can be divided into discrete source patches such that the activity of the entire cortex can be modeled by a finite set of dipoles, typically several thousand. The relationship between the current generated by a single dipole (the net current generated by all synchronous post-synaptic potentials in the corresponding patch) and a single scalp potential measurement is assumed to be linear. In other words, for a given source dipole and a given measured location on the scalp, there exists a scalar lead-field value. The voltage is measured at a scalp sensor (electrode), typically in microvolts, and the current is generated by the dipole, with a dipole moment typically expressed in nano-ampere × meter. For every dipole and sensor pair, there is a separate lead-field value, which is determined by the geometry and conductivities of the head tissues, the location of the dipole, and the location of the sensors. Together these several determining factors are collectively referred to as the *electric head model*.

1.1. Spatial sampling of the head surface potential field

The surface potential field is a continuous field that must be discretized for measurement. The Nyquist theorem of discretization states that the sampling rate must be twice as frequent as the highest frequency to be characterized in order to avoid aliased (mischaracterized) signals. Whereas temporal sampling is conducted with an analog-to-digital converter for the EEG time series, spatial sampling of the head surface potential field is conducted with the discrete electrodes of the 2D sensor array. The same principles of discretization apply to space as well as time. Adequate spatial sampling with a dense sensor array is necessary to avoid aliasing of spatial frequency, the variability of the potential field in space (Tucker, 1993; Srinivasan et al., 1998). Although it was traditionally assumed that the skull conductivity was so low that a few scalp sensors were sufficient to capture the relevant brain activity, recent in vivo studies show that the skull has more inter subject variability and may be in fact more conductive than previously assumed (Geddes and Baker, 1967; Oostendorp et al., 2000; Gonçalves et al., 2003; Gutierrez et al., 2004; Lai et al., 2005; Zhang et al., 2006), and therefore higher sampling density is required (Ryynänen et al., 2006) to prevent spatial aliasing. The influence of skull conductivities on EEG source localization has been examined systematically by a number of recent papers (Wang and Ren, 2013; Huiskamp et al., 1999; Song et al., 2013).

Recording from the adult head surface with a closely spaced (3 mm) sensor array has shown considerable high spatial frequency content, indicating the need for sensor spacing of 1 cm or less (Freeman et al., 2003). With neonates and infants, who have less resistive skulls and large openings (such as fontanels), smaller intersensor distances (between 0.6 and 1 cm) are required (Odabaee et al., 2013).

With whole head coverage in an optimal geodesic pattern, a 256-channel dense array provides ~2 cm sensor spacing for a medium sized adult head. To achieve ~1 cm intersensor distances, roughly 500 channels would be needed. Convergent evidence has come from analysis of the half-sensitivity volume, the region of the intracranial space for which sensitivity to source propagation is provided by the spacing of surface sensors (Malmivuo et al., 1997). With estimates of the skull:brain conductivity ratio of 15:1, half-sensitivity volume estimations suggest that approximately 500 channels are required for adequate spatial sampling of the human EEG (Malmivuo and Suihko, 2004; Ryynänen et al., 2004, 2006). Evidence derived from human studies (Luu et al., 2001; Odabaee et al., 2013) confirms these simulation studies, suggesting that spatial sampling may be sub optimal with EEG recordings with conventional electrode montages (less than 128 channels).

While spatial sampling density is important, *coverage* is also crucial. Often EEG data are obtained only from the top half of the head, due to the mistaken assumption that only electrodes adjacent to the brain are needed. This bias in coverage can lead to very poor estimates of activity from the inferior brain sources (Lantz et al., 2003; Sperli et al., 2006). Recently, Delorme et al. (2007) demonstrated the importance of including facial electrodes for localizing the source of the pre-motor P3f positivity. Although electrodes on face are more susceptible to EMG and movement artifacts, and thus require careful handling to be included in source estimation, considerable progress is being made in methods for removing this contamination (Fitzgibbon et al., 2013; Moretti et al., 2003; Gao et al., 2010; Shackman et al., 2009; McMenamin et al., 2011; Olbrich et al., 2011; Gross et al., 2013).

Considering these issues, the goal of the present study is to examine how source solutions are affected not only by sampling density but also by extending sampling coverage to include the inferior head. We therefore investigated the effect of sensor density and inferior head coverage on EEG source localization accuracy with simulated data whose sources were known, using an atlas model of the human head. We then constructed electric head models (finite difference models with high resolution tissue segmentation and conductivity estimation) using the MRI of specific individuals. With a normal individual's head model, we illustrated the lead field projections (from cortical sources to scalp electrodes) from oriented cortical sources. With an epileptic patient's individual head model, we examined the accuracy in localizing the source of epileptiform activity. We selected eight (whole 256-, 128-, 64-, 32-, upper 128-, 64-, 32-, 16-channels) coverage configurations based on the Geodesic Sensor Net, as well as the conventional International Ten-Twenty (10–20) and 10–10 electrode montages. The source reconstruction was performed using the minimum norm (MN (Dale and Sereno, 1993)) and Standardized Low Resolution Brain Electromagnetic Tomography (sLORETA (Pascual-Marqui, 2002)) linear inverse source estimation methods for each configuration. In the simulations, the accuracy of EEG source localization was assessed by comparing the estimated sources to the known sources. For the example of localizing epileptiform activity, the evidence of accurate localization was the convergence with intracranial recordings, as well as the successful suppression of seizures with neurosurgical resection of the epileptic focus.

2. Material and methods

The deidentified data from epileptic patients was obtained with approval of the Institutional Review Board of the University of Washington.

2.1. Forward problem

The forward problem, or volume conduction electrical head model, includes a set of conditions that specify the way that currents propagate from their site of generation at the cortex to the site of measurement at the scalp. The electrical forward problem calculates the distribution of the electrical potential on the surface of the head, given the positions, orientations and magnitudes of current sources, as well as geometry and electrical conductivity of the head volume (Mosher et al., 1999; Berg and Scherg, 1994;

Zhang, 1995; Hallez et al., 2007; He et al., 2002; Ary et al., 1981; Fuchs et al., 1998).

2.1.1. Head model construction

The electric head model is created to capture geometries of head tissues (the scalp or flesh, bone, cerebral spinal fluid (CSF), white matter, gray matter, air compartments, and eyeballs).

For the atlas model used in the present simulations, tissue compartments were constructed from the whole head MRI of a single subject Colin27 (http://www.bic.mni.mcgill.ca/ServicesAtlases/Colin27), whose head shape closely matches the MNI305 atlas, the Montreal Neurological Institute's 305-subject average MRI (http://imaging.mrc-cbu.cam.ac.uk/imaging/MniTalairach). For an accurate characterization of skull bone, we obtained a CT scan of this individual. The MRI and CT images were co-registered prior to segmentation of the brain and cerebral spinal fluid (identified from MRI data), and the skull and scalp (identified from CT images). The individual's MRI and CT images were then aligned with the brain volume from the MNI305 atlas with Talairach registration. The locations of the dipoles were derived following the method of Pascual-Marqui et al. (1994) by discretizing the gray matter volume of the MNI305 atlas. This resulted in 2447 dipole locations, each with three *triples* or *xyz* orthogonal orientations (7341 dipoles), with each source representing 7 mm^3 in volume.

For the individual electric head model of the patient, the T1-weighted scan was acquired using a Siemens MPRAGE sequence (repetition time (TR) = 2.5 s; echo time (TE) = 3.4 ms; flip angle (FA) = 8°) with a $1 \times 1 \times 1$ mm resolution covering 256 voxels in each spatial direction. EGI's BrainK software (Song et al., 2013) performed tissue segmentation, registration of the skull atlas (derived from a high-resolution CT image of the MNI atlas man: Colin27) to the individual's MRI, and registration of EEG sensor positions, derived from Geodesic Photogrammetry System (Russell et al., 2005) to the MRI scalp surface. The use of a CT atlas with X-ray attenuation values for each voxel of the skull is a proprietary EGI method (Tucker and Tucker, 2003). Tissue segmentation was performed to identify the following tissues: eyeball, scalp/fresh, skull, air, cerebral-spinal fluid (CSF), gray matter (GM) and white matter (WM).

To create oriented dipole positions for the individual head model, the cortical surface was first characterized through a relative thresholding algorithm (Li et al., 2006, 2011), in the form of triangular meshes, which were tessellated into patches of approximately equal size. All models used in the present study contained ~1000 dipoles (i.e., patches) per hemisphere. Each patch was about 1 cm^2. For each patch, orientation vectors perpendicular to each vertex within the patch were averaged to derive the average dipole orientation (vector sum) for that cortical patch.

2.1.2. Lead fields calculation and numerical implementation

Lead fields are defined as forward projections of unit magnitude dipole moments from cortex to scalp sensors. They consist of a lead field matrix (LFM) describing the projection from each of N_v dipoles to each of N_e sensors. A generic LFM for a given subject head volume can be calculated first for more dense coverage of scalp (several thousand points) and then potentials for session specific sensor locations interpolated from this generic LFM on scalp. It can be accomplished by the "brute force" approach launching separately the forward solver for each dipole position. However, one can reduce the required number of forward solutions drastically by using the reciprocity principle for LFM calculations (Hallez et al., 2007; Malony et al., 2011). We have implemented both these approaches as they can be parallelized effectively in a multi-core cluster environment or desktops with modern Graphic Processing Units (GPUs: http://www.gpgpu.org/).

Mathematically, the electrical forward problem is solving the quasi-static approximation of Maxwell's equations, the Poisson equation (Smith et al., 2012):

$$\nabla \cdot (\sigma \nabla it\phi) = S, \text{ in } \Omega \quad (1)$$

with no-flux Neumann boundary conditions on the scalp:

$$\sigma(\nabla it\phi) \cdot n = 0, \text{ on } \partial\Omega \quad (2)$$

Here Ω is the head volume, $\partial\Omega$ is the surface of the head (scalp), $\sigma = \sigma_{ij}(x, y, z)$ is an inhomogeneous tensor of the head tissues conductivity and $S = -I\delta(r - r_+) + I\delta(r - r_-)$ is the source current configuration constructed in the simplest case from a source and a sink of strength I at the vector locations r_+ and r_-, and n is the boundary normal.

The conductivity values were set to 0.44 (S/m, scalp), 0.018 (S/m, skull), 1.79 (S/m, CSF), and 0.250 (S/m, brain) to reflect recent evidence that the skull-to-brain conductivity ratio is about 14:1 (Oostendorp et al., 2000; Gonçalves et al., 2003; Ryynänen et al., 2006; Zhang et al., 2006; Ferree et al., 2000), in contrast with the 80:1 ratio traditionally assumed (Rush and Driscoll, 1969; Geddes and Baker, 1967).

Numerically, we built a finite difference forward problem solver for the volume conduction based on the multi-component alternating directions implicit (ADI) algorithm (Salman et al., 2008; Turovets et al., 2008; Malony et al., 2011; Song et al., 2013). The numerical method is a generalization of the classic ADI algorithm, but with improved stability in 3D. We chose the FDM (Huiskamp et al., 1999; Ida, 2015), approach over FEM (Jin, 2002) and BEM (Gaul et al., 2012) methods for its simplicity of implementation from the MRI/CT tissue segmentation map that produces a cubed lattice of nodes. Therefore, meshes are easy to construct (once segmentation is accomplished) as the cubic/rectangular elements can be mapped directly from the voxels of the medical images (3D MRI/CT scans), including all relevant anatomical details in contrast to BEM and FEM.

To set up the boundary conditions in the heterogeneous biological media within a complex geometry like the human head, the method of the embedded boundaries is used in FDM. Here an object of interest is embedded into a cubic computational domain with extremely low conductivity values in the external complimentary regions. This effectively guarantees there are no current flows out of the physical area (the Neumann boundary conditions are naturally satisfied). The forward computations using high resolution structural models (1 mm in the present case) and multiple forward solutions, represent computationally intensive tasks and require high performance computing. The electrical forward and inverse conductivity optimization models have been implemented in a parallel C/C++ code (OpenMP and MPI) and CUDA to run on multi-core cluster and GPGPU platforms (Salman et al., 2015).

2.2. Inverse problem

The inverse problem requires mapping the recorded surface potentials to the cortical sources space of the volume-conductor model; this is problematic for EEG because it is highly underspecified or mathematically ill-posed. There are diverse methods (Grech et al., 2008; Baillet et al., 2001; Yao and Dewald, 2005) for handling this ill-posed problem, such as equivalent current dipole (Fuchs et al., 1998), MUSIC (Mosher et al., 1998; Mosher and Leahy, 1999), Beamforming (Veen et al., 1997), EPIFOCUS (de Peralta-Menendez et al., 2004) and distributed source localization (Minimum Norm (Dale and Sereno, 1993), LORETA (Pascual-Marqui et al., 1994), LAURA (Michel et al., 2004), sLORETA (Pascual-Marqui, 2002)). In this study, MN and sLORETA were chosen to investigate the relationship between the number and coverage of electrodes and EEG source localization.

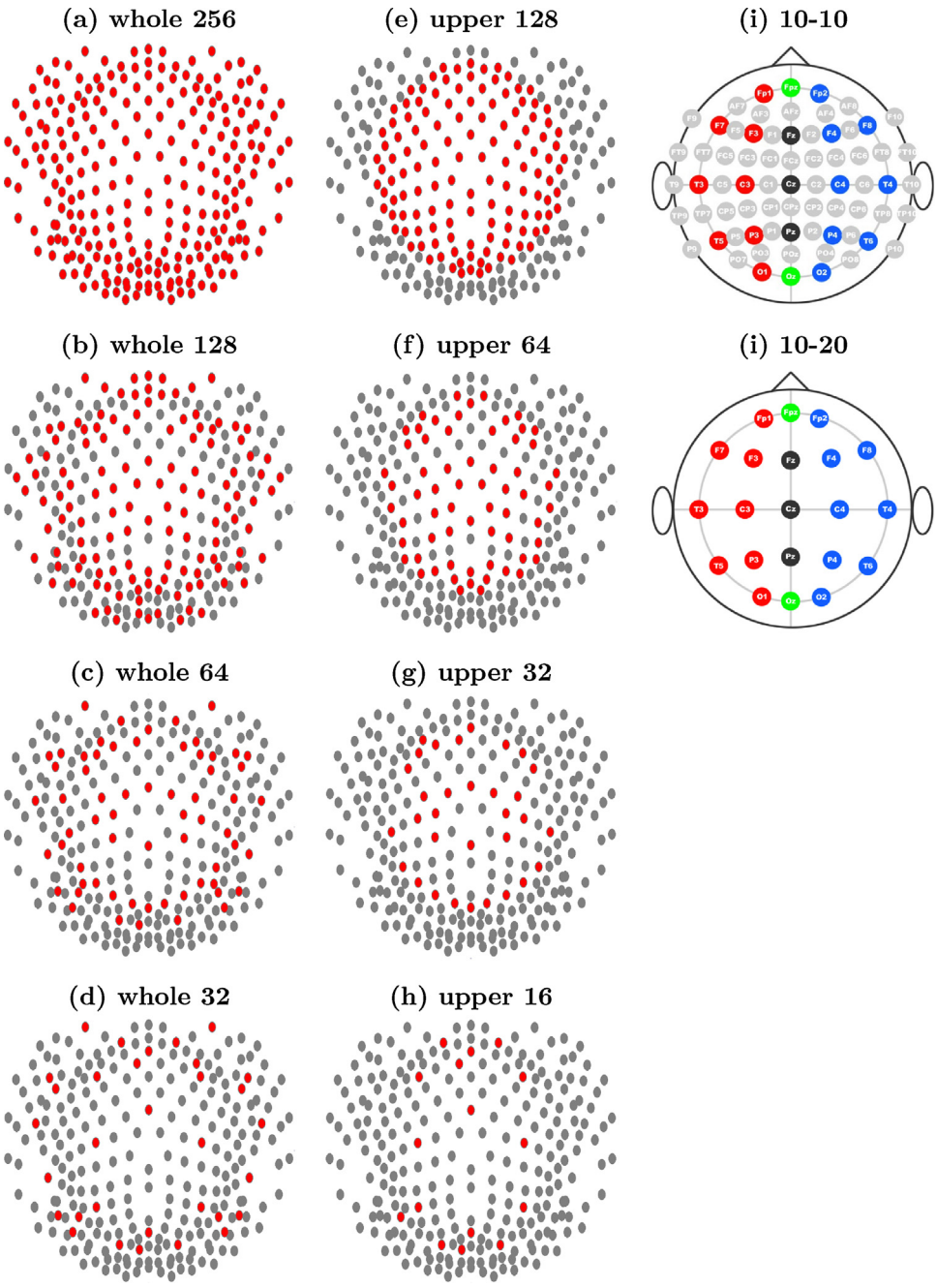

Fig. 1. Sampling density and coverage of arrays derived from the Hydrocel Geodesic Sensor Net and International 10-10 and 10-20 systems. Gray dots are 256 sensors. Red dots are sensors used for the source localizations. (For interpretation of the references to colour in this figure legend, the reader is referred to the web version of this article.)

The EEG signal $\Phi(t)$ measured from N_e channels can be expressed as linear combinations of N_v dipoles $J(t)$:

$$\Phi = K \cdot J + E \tag{3}$$

where K is the lead field matrix and $E(t)$ is the additive noise with covariance matrix C_ε. Since the EEG inverse problem is ill-posed ($N_e \ll N_v$), mathematical and physical constraints are added to obtain unique solutions. Here we examined the MN and sLORETA inverse estimation methods. The solution for the inverse problem is

$$\hat{J} = arg\min_J\{\|\Phi - KJ\|^2 + \alpha\|J\|^2\}, \tag{4}$$

where α is the regularization parameter which controls the influence of the constrains relative to minimizing the residual of the fit, and $\|\cdot\|^2$ represents the square of the l_2-norm.

The MN solution is

$$\hat{J}_{MN} = T(\alpha)\Phi \tag{5}$$

where $T(\alpha) = K^T[KK^T + \alpha C_\varepsilon]^{-1}$.

The electrode potential variance C_Φ is a function of the actual source distribution covariance C_J and C_ε as

$$C_\Phi = KC_JK^T + C_\varepsilon. \tag{6}$$

The covariance of the estimates source distribution, $C_{\hat{J}}$ is given by

$$C_{\hat{J}} = T(\alpha)C_\Phi T(\alpha)^T = K^T[KK^T + \alpha C_\varepsilon]^{-1}K. \tag{7}$$

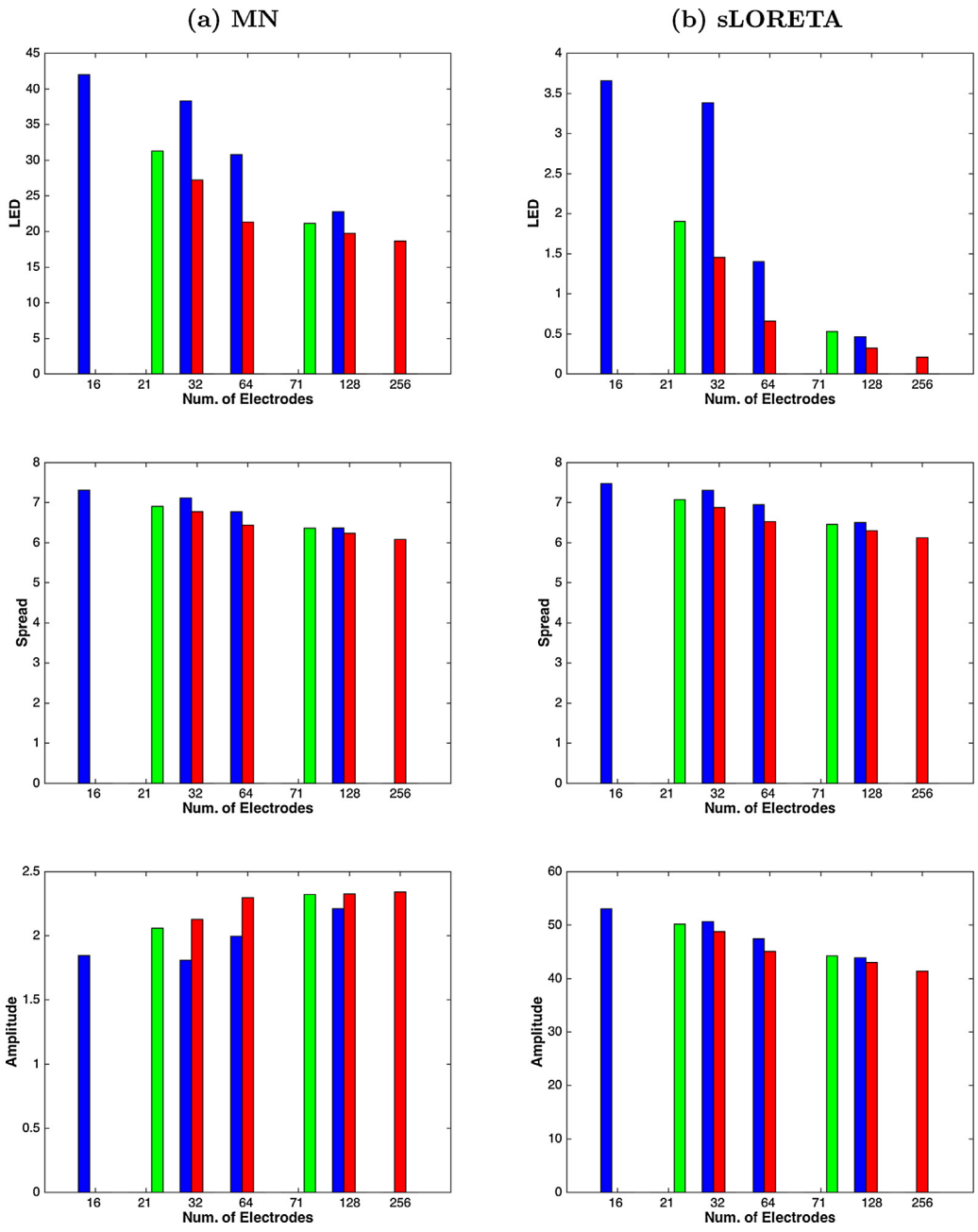

Fig. 2. LED, Spread and Amplitude as a function of sampling density and coverage with simulated data. (a) MN, (b) sLORETA red is whole head coverage, blue is upper head coverage and green is 10–10 and 10–20 systems. (For interpretation of the references to colour in this figure legend, the reader is referred to the web version of this article.)

For sLORETA, the standardization uses the diagonal $C_{\hat{J}}$:

$$\hat{J}_l^* = [C_{\hat{J}}]_{ll}^{-1/2}\hat{J}_l, \text{for } l = 1, \ldots, N_v \tag{8}$$

The accuracy of the solution depends on the choice of the hyperparameter α. The hyperparameter α controls the confidence between the fitting of the model $\Phi - KJ$ and the priors on the solution J. In general, the degree of regularization α increases with the noise level of the data. A simple method to estimate α is to plot the norm of the regularized solution $\rho = \|\hat{J}_\alpha\|$ vs the norm of the residual vector $\eta = \|\Phi - K\hat{J}_\alpha\|$ for the different values of α. The curve usually has an L-shape (Abascal et al., 2008). A satisfactory α is the inflection point of the curve. The corner of the L-curve corresponds to the optimum regularization parameter. The curvature $\kappa(\alpha)$ of the L-curve is

$$\kappa(\alpha) = \frac{\rho'\eta'' - \rho''\eta'}{(\rho'^2 - \eta'^2)^{3/2}}. \tag{9}$$

The optimal corner has the highest curvature (kappa).

2.3. EEG electrode sampling density and coverage

The sensor positions were defined by the average positions of the 256-channel Geodesic Sensor Net (Electrical Geodesics, Inc.) as well as the conventional measurement of the International Ten-Twenty System (21 sensors) and the 10–10 subdivision (71 sensors). To derive the 128-, 64-, and 32-channel positions for the Geodesic Sensor Net, the average positions of the 128-, 64-, and

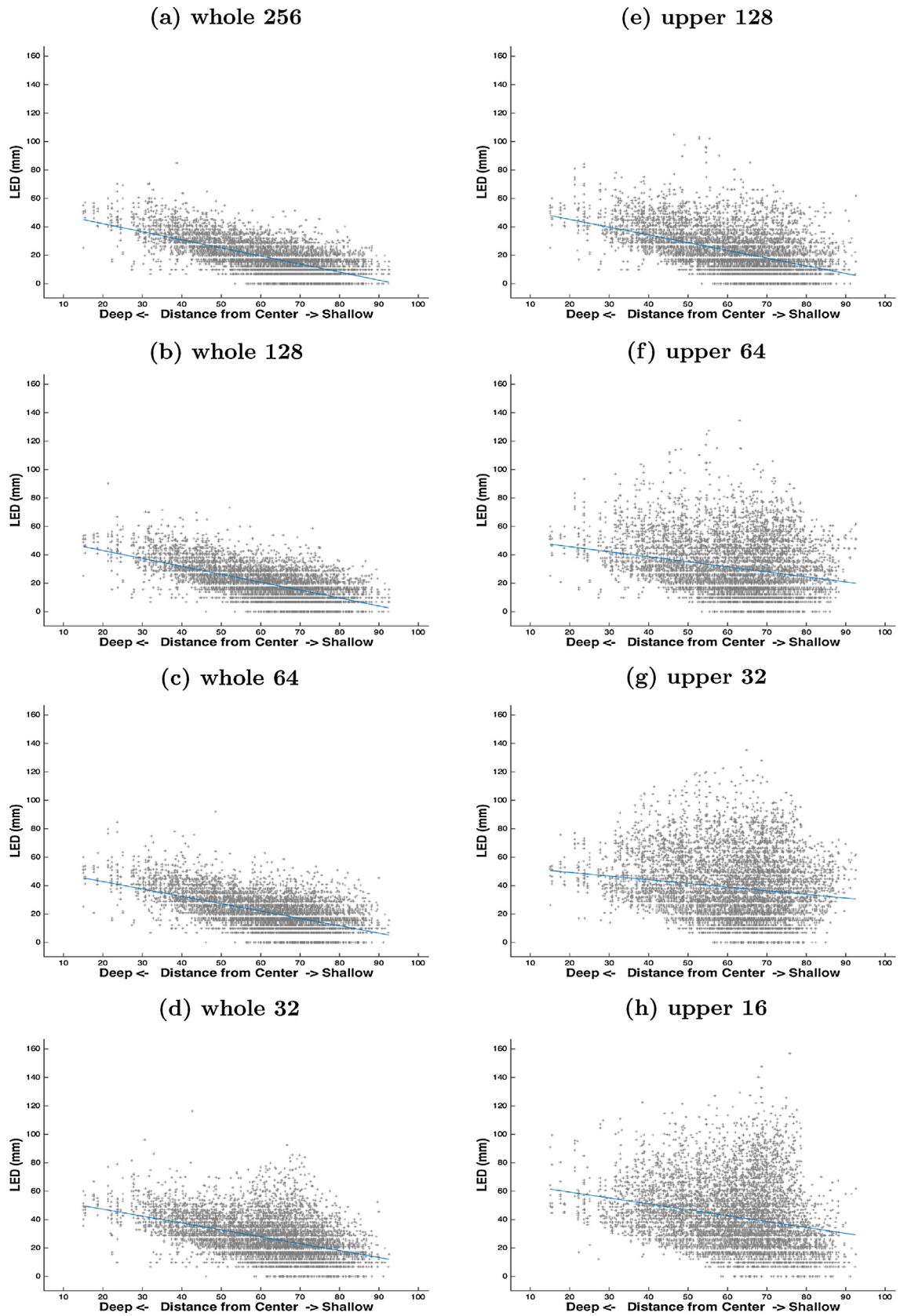

Fig. 3. LED vs depth of a dipole with minimum norm (MN) inverse. (a–d) Whole-head sampling and (e–h) upper-head sampling. Blue line represents the regression line of LED against the depth of dipoles.

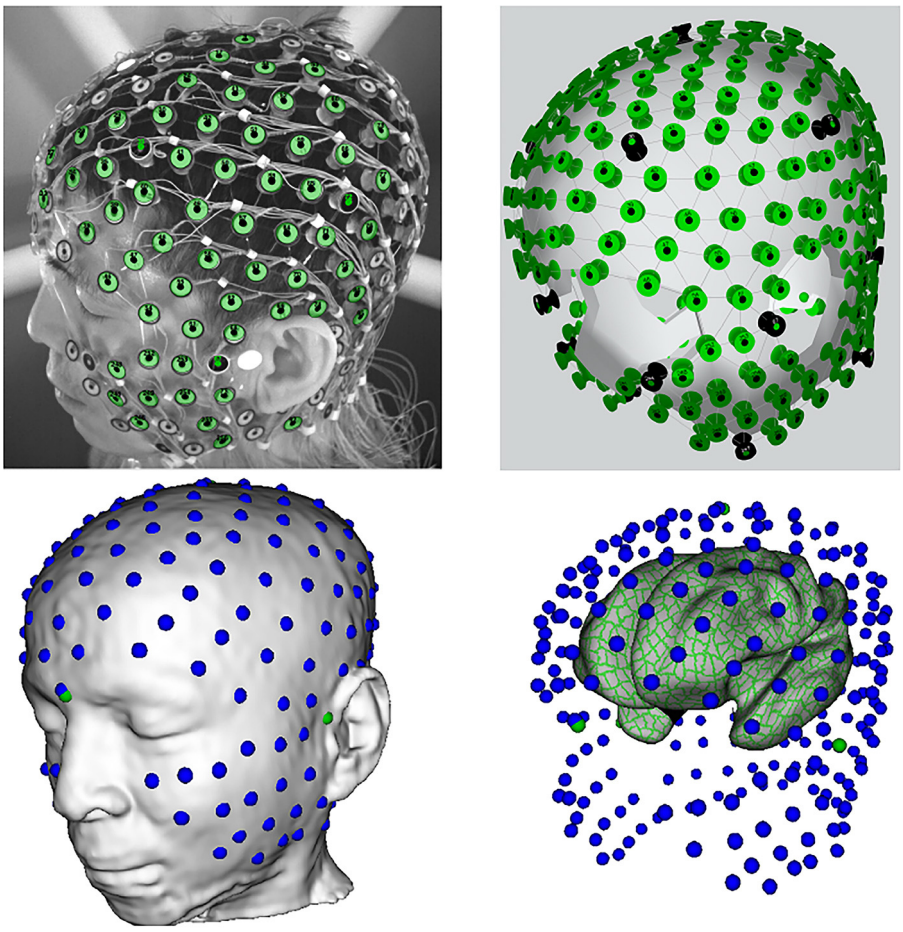

Fig. 4. Top left: positions of 256 sensors detected with photogrammetry (green) in the infrared image of the subject's head. Top right: computational model of these 3D sensor positions. Bottom left: registration of these 3D sensor positions with the subject's MRI head surface. Bottom right: schematic of the subject's brain inflated to visualize sulcal as well as gyral surfaces, and shrunk to fit the braincase. (For interpretation of the references to colour in this figure legend, the reader is referred to the web version of this article.)

Table 1
Localization error distance (LED), Spread, and Amplitude as a function of head models, inverse method, coverage, the number of channels, the mean of intersensor distances (ISD)

Inverse Method	Coverage	Channel Count	Mean ISD (cm)	LED (mm) Mean (SD)	Spread (mm) Mean (SD)	Amplitude Mean (SD)
MN	Whole	256	2.0	18.42 (11.34)	6.08 (0.56)	2.34 (0.67)
		128	2.7	19.73 (11.39)	6.23 (0.53)	2.32 (0.66)
		64	3.3	21.31 (11.57)	6.43 (0.51)	2.29 (0.66)
		32	5.37	26.99 (13.55)	6.77 (0.50)	2.12 (0.64)
	Upper	128	2.0	22.73 (14.64)	6.36 (0.72)	2.21 (0.74)
		64	2.7	30.83 (19.06)	6.77 (0.82)	1.99 (0.77)
		32	2.2	38.50 (21.78)	7.11 (0.84)	1.81 (0.78)
		16	5.37	41.04 (22.20)	7.30 (0.70)	1.84 (0.70)
	10–10	71		21.13 (12.07)	6.36 (0.55)	2.32 (0.68)
	10–20	21		31.28 (15.39)	6.90 (0.58)	2.05 (0.68)
sLORETA	Whole	256	2.0	0.20 (1.27)	6.12 (0.37)	41.41 (11.43)
		128	2.7	0.32 (1.60)	6.29 (0.34)	43.03 (11.87)
		64	3.3	0.66 (2.38)	6.52 (0.32)	45.08 (12.44)
		32	5.37	1.45 (3.71)	6.87 (0.32)	48.77 (13.95)
	Upper	128	2.0	0.46 (1.98)	6.50 (0.39)	43.89 (13.71)
		64	2.7	1.40 (3.68)	6.94 (0.35)	47.44 (17.10)
		32	2.2	3.38 (6.48)	7.30 (0.35)	50.63 (20.75)
		16	5.37	3.65 (6.32)	7.47 (0.38)	53.10 (18.72)
	10–10	71		0.53 (2.08)	6.45 (0.34)	44.25 (12.36)
	10–20	21		1.90 (4.36)	7.07 (0.37)	50.17 (15.51)

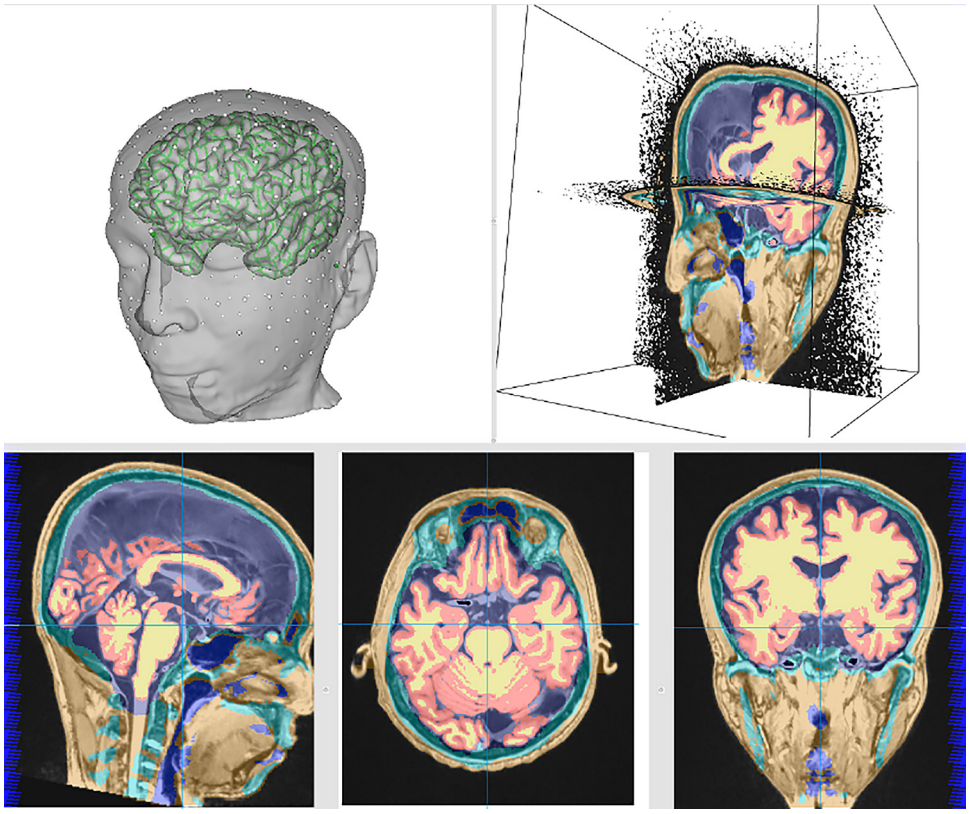

Fig. 5. Segmentation of tissues for the finite difference model for the subject in Fig. 4. Top left: registration of 256 sensors with the MRI head surface (with the surface set to translucent to visualize the relationship to the cortical surface). Top right: slice views through the segmented volume. Bottom: sagital, axial, and coronal slices showing tissue segmentation, with gold = flesh, turquoise = bone, light blue = CSF, dark blue = air, red = gray matter, yellow = white matter, gray = eyeball. (For interpretation of the references to colour in this figure legend, the reader is referred to the web version of this article.)

32-channel HydroCel Net were registered to 256-channel HydroCel Net and then the closest position from the 256-channel array was chosen for each channel. Fig. 1 shows the positions of the sensors for each channel count, illustrating sampling density as well as coverage.

To compare these results with conventional EEG electrode systems, the 10–20 and 10–10 positions were determined by conventional measurement (percentages from arcs of nasion to inion, periauricular points to vertex) of a subject wearing the 256 Net, and the closest of the 256 positions was selected for each 10–20 or 10–10 position.

Coverage (whole head vs upper) was defined for each Geodesic Sensor Net channel density as those channels in the upper half of head coverage as approximately demarcated by the cantho-meatal line. For the 10–20 and 10–10 montages, the entire montage was used (given the there are no channels on the face and neck for either of these montages).

2.4. Simulated data

The simulated EEG data were created by forward projection from atlas cortical triples (each source with x, y, z vectors) to scalp sensors in the LFM with additive Gaussian noise of 10% SNR (signal-to-noise-ratio).

With the simulated data based on 7341 forward projections with 3 orientations at 2447 locations, the location and orientation of the source for each scalp topography is known. Therefore, we quantified the source reconstruction with the evaluation metrics (Hauk et al., 2010). The localization error distance (LED) is defined as the Euclidean distance (mm) between the location of the maximum current distribution from the inverse solution and the position of the true generating dipole: $LED_j = ||x_j - x_p||$, where x_j is the true coordinate and x_p is the peak coordinate. Small LED values represent small errors. Spatial spread (Spread) is defined by: $Spread_j = \sqrt{\frac{\sum_i d_{ij} F_{ij}^2}{\sum_i F_{ij}^2}}$, where F_{ij} is the source distribution of dipole J activated and d_{ij} is the distance between dipole I and J. A large value on this metric indicates a more widely distributed solution. The overall amplitude is defined by $Amp_j = \sum_i |F_{ij}|$. All metrics (LED, Spread, Amplitude) were computed at 7341 forward projections and averaged over 7341 forward projections in Table 1 and Fig. 2.

2.5. Interictal spike data

Previous research has shown that interictal spikes are often useful in localizing the seizure onset zone (Brodbeck et al., 2011). To investigate the spatial sampling and coverage effects on source estimation with real data, we localized the onset of averaged interictal spikes from an epileptic patient, where the seizure onset zone was known from intracranial recordings and surgical outcome. In this patient, intra-cranial EEG (icEEG) identified the right anterior temporal lobe as the seizure onset zone and the locations was further confirmed by clinical outcome (seizure free, Engel Epilepsy Surgery Outcome of I (Engel, 1993)).

The dEEG data from this patient were acquired with a 256-channel array Geodesic Sensor Net (EGI, Eugene, OR) using Net Station 4.5 software. All electrode impedances were below 70 kΩ before recording was started. Recordings were referenced to the vertex electrode. The data was digitized with a 16-bit A/D converter at a 250 Hz sampling rate. The data were reviewed by an epileptologist to identify spikes. Similar spikes (based on morphology and spatial topography, $n = 56$) were segmented into 400-ms epochs

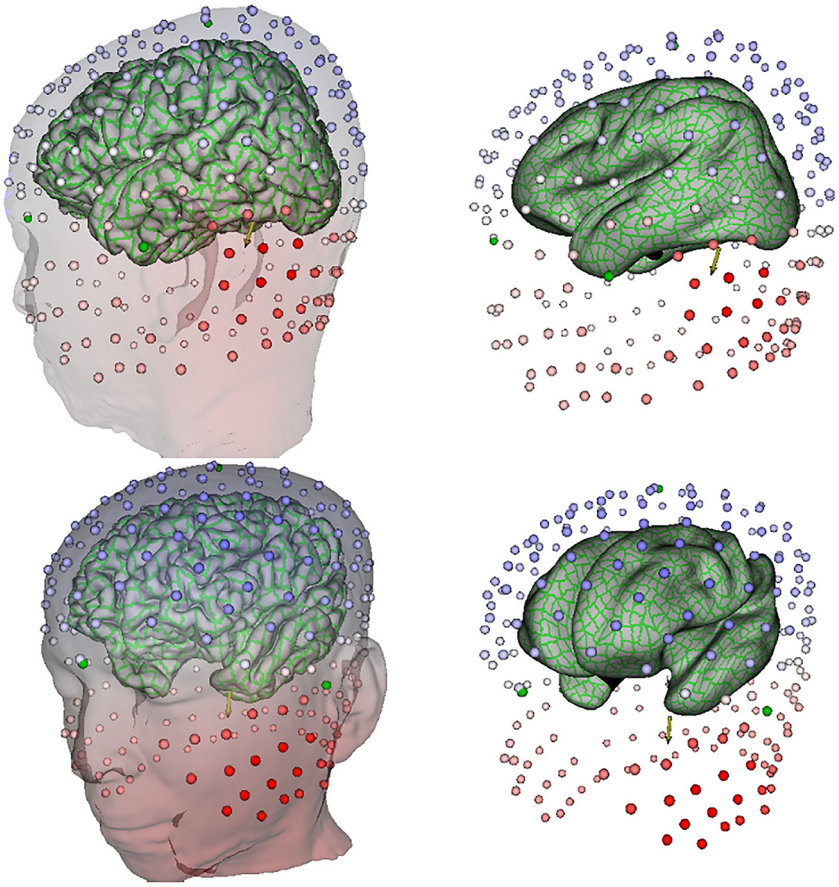

Fig. 6. Examples of lead field projections of oriented dipoles from cortical surface patches on the basal surface of the brain. Top: cortical-surface-positive source dipole (yellow arrow) in the left fusiform region. The positive field (red) is captured by the electrodes behind the left ear and on the neck, whereas the negative field (blue) is distributed diffusely over the top of the head. Bottom: cortical-surface positive dipole in the anterior left temporal lobe. The positive field (red) is captured largely by the inferior left cheek electrodes, whereas the negative field (blue) is again distributed diffusely over the top of the head. (For interpretation of the references to colour in this figure legend, the reader is referred to the web version of this article.)

centered on the spike peaks, and averaged to derive a homogenous, average spike topography for that patient's spike type. Sensor configurations for the sparser arrays were generated by subsampling the 256-channel array.

Global field power (GFP) (Lehmann and Skrandies, 1980) was calculated over the average spike epoch, and source localization was performed at spike onset, defined as the time point corresponding to the half-max of the rising slope of the GFP from the baseline to spike peak (Fig. 7). The spike onset zone was localized using MN and sLORETA and a 95% intensity threshold was applied to the display of all source activity maps.

3. Results

3.1. Simulations

3.1.1. Effect of sampling density and coverage on localization error

Table 1 and Fig. 2 present summary statistics for each inverse method, head model, EEG channel count (i.e., sampling density as defined in Fig. 1), and coverage of the simulated data with noise. As expected, results show that as sampling density increases, localization errors decrease, regardless of the inverse method, head model. As shown in Fig. 2, the decrease is asymptotic, such that source localization is inaccurate for 16 or 32 channels, marginal for 64 channels, becomes reasonably accurate for 128 channels (15–20 mm error), and only increases slightly for 256 channels with the atlas model.

In each of the atlas model simulations, whole-head coverage produces smaller errors than upper coverage given the same number of sensors. Similar to the sampling density results, the coverage results show that as coverage increases, localization errors decrease regardless of inverse method.

In general, sLORETA is better method to achieve the accurate source localizations than MN since the averages of LEDs for sLORETA are smaller than ones for MN. The averages of spreads are not significantly different by density and coverage of electrodes regardless of source localization methods.

3.1.2. Effect of sampling density and coverage on localization error as a function of dipole depth

An important consideration for source estimation of scalp recorded voltage data is the ability to accurately estimate both superficial and deep sources with minimal error. Fig. 3 presents LEDs for the minimum norm as a function of sensor sampling density, and coverage as a function of source depth. The depth of the source is defined by distance from the center of the head to the source location (the higher the depth value, the more superficial the source location). MN is only good for shallow sources since MN is biased to the shallow sources. LEDs of MN are not different for dipole orientations but for dipole locations. For MN, deep sources have higher LEDs than shallow sources in Fig. 3. But orientations are not significantly different. For sLORETA, both dipole orientations and locations are not different in LEDs.

The benefit of whole-head coverage is apparent in these simulations. Compare Fig. 3b (128 whole head) vs Fig. 3e (128 on top of

head). Errors are reduced considerably for the same channel density when sensors are distributed as evenly as possible across the whole head surface, including the face and neck.

3.1.3. Lead field projections of cortical surface patches in the individual electric head model

A major constraint on the ambiguity of the source localization is applied when the individual's cortical surface is known, and the cortical surface orientation can be included as well as the exact sensor positions. Fig. 4 illustrates the location of sensors in infrared images, their images, their 3D localization with photogrammetry, and the positions of the sensors when registered with the individual's structural MRI. The infrared images are used to derive the 3D position of each EEG sensor on the scalp surface. The sensor coordinate map is important for increasing the accuracy of head model, relative to the default positions, as it describes the true position of the EEG sensors relative to the whole head.

Fig. 5 shows the segmentation of the major head tissues for this individual, with each tissue assigned to an appropriate electrical conductivity. To examine the lead field projections from patches of cortical surface, particularly on the basal surface of the brain, we selected two patches of cortex in the inferior left hemisphere from the normal subject in Figs. 4–6, one in the fusiform area (Fig. 6, top) and the other at the temporal pole (Fig. 6, bottom), and computed the lead field projections from these two equivalent dipoles. Although the lead field projections are determined by the complex geometries and conductivities of the tissues in the FDM shown in Fig. 5, the results of these simulations are clearly dominated by the orientation of each cortical patch, which is highly unique for each individual. As this example illustrates, immediately adjacent cortical patches create highly divergent lead field projections to the surface electrodes, solely as a function of the idiosyncratic orientation of the cortex at each patch.

3.2. Interictal spike data

Fig. 8 shows the source localization results for the rising edge of an averaged epileptic spike, estimated with the MN and sLORETA as a function of coverage and sampling density. The localization of spike onset with the whole-head coverage with 256, 128, 64, and 32 channels showed the strongest activity at the right anterior temporal lobe with MN (Fig. 8a). Whole-head coverage at 256, 128 and 32 channels with sLORETA also localized the activity to the right anterior temporal lobe (Fig. 8b).

For the upper head coverage, the source activity was clearly mislocalized, predominantly to the right superior frontal lobe with MN and the right inferior frontal lobe with sLORETA. MN source estimations incorrectly localized to the right superior frontal region due to the fact that the MN source estimations are biased toward the shallow source distributions, as seen in Fig. 8. The tendency for source solutions to mislocalize to the right inferior frontal region in sLORETA seems to be due to the fact that the spike focus at the scalp has a ventral distribution. The whole-head coverage with 64-channels, and all the sampling densities using only the upper head surface, mislocalize this scalp distribution.

4. Discussion

There is increasing recognition that adequate spatial sampling of the head surface potential field is needed to support accurate electrical source estimation of human brain activity (Lantz et al., 2003; Laarne et al., 2000; Luu et al., 2001; Malmivuo and Suihko, 2004; Nunez and Srinivasan, 2005; Ryynänen et al., 2006; Srinivasan et al., 1998; Hassan et al., 2014; Song et al., 2014). Increasing evidence from simulation and empirical measurements now shows

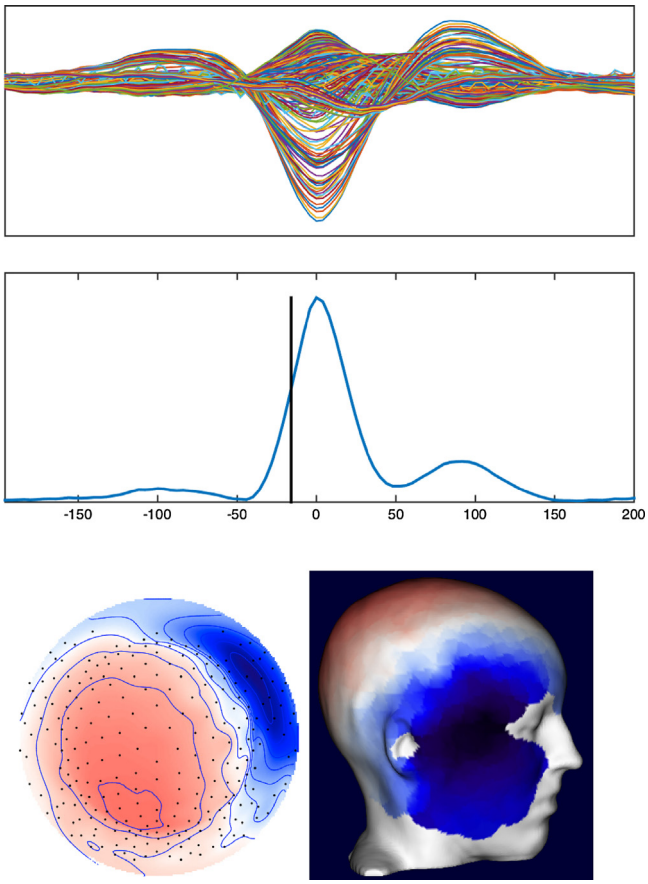

Fig. 7. Spike Onset localized in a patient's individual head model. (Top) 256-channel butterfly plot of average spike waveforms from −200 ms to 200 ms around spike peak and global field power. Black bar indicates time of spike onset used in source localization. (Bottom) Average spike scalp topography at onset.

that increasing the number of recording channels provides greater accuracy in source estimation. As Sohrabpour et al. (2015) have recently reported, the results are poor with less than 64 channels, improve with higher densities, and yet as the number of channels is increased further the improvement is asymptotic. These results are consistent with the present findings shown in Table 1 and Fig. 2, including the observation that the improvement from 128 to 256 channels is modest.

However, there is less recognition in the current literature of the importance of adequate coverage, specifically the sampling of the inferior head regions. If 128 channels are concentrated on the top of the head, a 2 cm intersensor distance may be approached. However, with the improved coverage of the face and neck with the Geodesic Sensor Net, the 2 cm intersensor distance is achieved only with 256 channels.

One issue limiting coverage of the face and neck in previous studies is the fact that the lower head has been difficult to sample with traditional electrode placement techniques, such as cloth caps, that apply pressure primarily to the top of the head. Another issue has been the misconception that EEG cannot be recorded from more inferior sites, such as the face. Modern sensor placement schemes, such as the five-percent system (Oostenveld and Praamstra, 2001) or the geodesic placement system (Tucker, 1993) now include sensors on the inferior head surface. In fact, with these modern placement schemes, electrodes on the face can be considered to serve the same purpose as sphenoidal or mandibular electrodes, which is to record activity from the medial and basal temporal regions (Feng et al., 2015). In the present simulation results, including both the atlas model source reconstructions

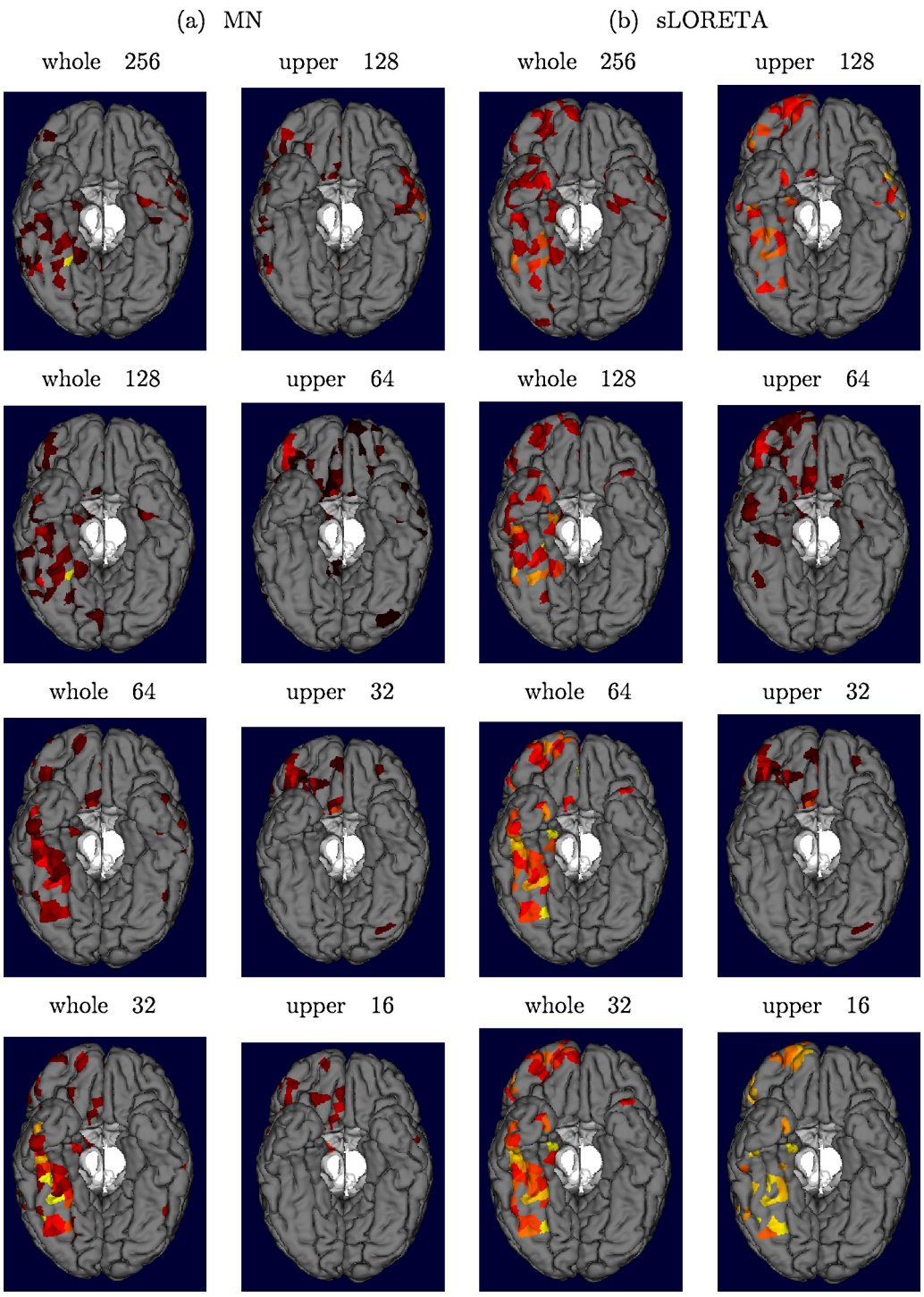

Fig. 8. Spike Onset localized in a patient's individual head model with MN and sLORETA. (a) MN and (b) sLORETA source distributions with different sensor distributions. The right anterior temporal lobe was independently identified as the epileptogenic spike onset from intracranial data (and surgical outcome). Whole samples with MN and sLORETA are correctly localized.

and the individual head model lead field projection examples, the importance of sampling the inferior regions of the head was evident. For the present example of localizing an epileptic spike, the inferior head channels were clearly important in measuring the field distribution of the pathological brain activity.

In the systematic atlas simulations and source reconstructions (Table 1 and Fig. 2), the results suggested that whole-head coverage improved source localization accuracy above and beyond the improvements obtained by dense sampling of the superior head surface. When compared to source estimates obtained with data sampled only from the upper surface of the head, whole-head coverage reduced both localization errors and variability of the errors, regardless of sampling density and inverse technique (Figs. 2 and 3). Furthermore, even for superficial brain sources, for which the spatial frequency information is relatively high, errors associated with undersampling of the spatial frequency content can be compensated somewhat by inferior coverage. That is, as seen in Table 1 and Figs. 2 and 3, particularly for superficial and mid depth sources, the errors for whole-head coverage were always smaller compared to errors for upper coverage only, even at low channel counts.

Intuitively, these three findings can be understood in relation to the zero-surface integral (Perrin et al., 1990; Yvert et al., 1997). When the whole surface of the volume (head) is sampled, the surface integral potential of each dipole will be zero (as positive and negative fields are summed). Because this occurs regardless of the number of dipoles, whole surface sampling ensures that the net energy is zero, and that an even balance of positive and negative fields of cortical sources has been included in the inverse estimation. This assurance of approximating the zero surface integral is important for both deep and superficial sources. The source solutions obtained using sLORETA show that although the superficial bias is dramatically attenuated with this constraint compared to the minimum norm, the addition of data from the inferior surface also improves the accuracy of source estimates for very deep sources.

4.1. Limitations

We limited the simulations to the minimum norm class of inverse methods (MN and sLORETA). We expect that inferior head surface sampling will similarly benefit other techniques as well (e.g., (Wipf et al., 2010)). The sLORETA is a popular inverse method with "zero localization error in the absence of noise" (Pascual-Marqui, 2002). Contrarily to MN, sLORETA is not the intensity estimation but rather the probability of this source distribution. With sLORETA standardization, if there is an exact match between the head parameters (geometry & conductivity) that generate the head surface potentials and the head model that is employed for the forward model, sampling density and coverage does not matter, and perfect (with no noise) source reconstruction is guaranteed. This is obviously a trivial result, because the exact electric head model is not known for actual human heads. In practice, there is always some mismatch between the human head propagating the EEG and the head model used for source reconstruction, and that mismatch guarantees that the sLORETA estimation will be flawed. With increasing accuracy of head conductivity models that match the individual subject, standardization methods (like sLORETA) may become defensible.

Another limitation of the current study is that we did not assess the impact of noncephalic artifacts in the data, and these are particularly problematic for the sensors on the face. Source analysis methods are generally inaccurate if the data is confounded with artifact, such that it is important to minimize artifacts during acquisition and to apply appropriate artifact identification and cleaning methods during post-processing. These considerations are particularly important for data on the face and neck.

Finally, an important limitation is that the simulations of density and coverage were conducted with atlas triples (estimating *xyz* moments for each source), largely because these atlas results can be generalized to head models of many people. In contrast, even the simulation results with an individual's oriented cortical sources are restricted to that individual. Nonetheless, the example lead fields computed with oriented cortical surface dipoles and the individual head model (Figs. 4–6) illustrated the sensitivity of the head surface potentials to the orientation of each cortical patch. It will be important in future research to construct enough individual head models, including cortical surface reconstruction with oriented dipole patches, to allow general conclusions on the limits of electrical source estimation when the orientation of the cortex is known.

5. Conclusions

Systematic comparisons of varying sensor sampling density and coverage of the surface of the head showed that error in electrical source estimation can be reduced by using a sufficient number of EEG sensors (128 or 256) as well as by distributing these over inferior head regions (including the face and neck) as well as the top of the head. These factors remained important in the presence of random noise added to the simulated data. Whereas improved precision can be obtained by physical modeling of head tissue conductivity in the geometry of the individual's MRI, the orientation of the individual's cortex has a major influence on the head surface projections of the source fields. The importance of characterizing the individual's cortex was illustrated here by two examples of cortical patch lead field projection from sources in the basal temporal lobe. An example of localizing an epileptic spike illustrated the clinical importance of whole head sampling. In this patient, as in many others, the epileptiform activity was localized to the temporal lobe, such that inferior head electrodes were necessary for adequate sampling of the head surface field.

Acknowledgments

Electrical Geodesics, Inc., provided support in the form of salaries of authors.

References

Michel CM, Lantz G, Spinelli L, de Peralta RG, Landis T, Seeck M. 128-Channel EEG source imaging in epilepsy: clinical yield and localization precision. J Clin Neurophysiol 2004];21(2):71–83.
Lantz G, de Peralta RG, Spinelli L, Seeck M, Michel C. Epileptic source localization with high density EEG: how many electrodes are needed? Clin Neurophysiol 2003];114:63–9.
Holmes MD. Dense array EEG: methodology and new hypothesis on epilepsy syndromes. Epilepsia 2008];49:3–14.
Brodbeck V, Spinelli L, Lascano A, Wissmeier M, Vargas M, Vulliemoz S. Electroencephalographic source imaging: a prospective study of 152 operated epileptic patients. Brain 2011];134:2887–97.
Brunet D, Murray MM, Michel CM. Spatiotemporal analysis of multichannel EEG: CARTOOL. Comput Intell Neurosci 2011];2011:813870, doi:10.1155/2011/813870.
Dale AM, Sereno MI. Improved localization of cortical activity by combining EEG and MEG with MRI cortical surface reconstruction: a linear approach. J Cognit Neurosci 1993];5:62–176.
Delorme A, Westerfield M, Makeig S. Medial prefrontal theta bursts precede rapid motor responses during visual selective attention. J Neurosci 2007];27(44):11949–59.
Hassan M, Dufor O, Merlet I, Berrou C, Wendling F. EEG source connectivity analysis: from dense array recordings to brain networks. PLOS ONE 2014];9:e105041.
Jasper HH. Report to committee on clinical examination in EEG. Electroencephalogr Clin Neurophysiol 1958];10:370–1.
Tucker DM. Spatial sampling of head electrical fields: the Geodesic Sensor Net. Electroencephalogr Clin Neurophysiol 1993];87:145–63.
Srinivasan R, Tucker DM, Murias M. Estimating the spatial Nyquist of the human EEG. Behav Res Methods Instrum Comput 1998];30:8–19.
Geddes LA, Baker LE. The specific resistance of biological material–a compendium of data for the biomedical engineer and physiologist. Med Biol Eng 1967];5(3):271–93.
Oostendorp TF, Delbeke J, Stegeman DF. The conductivity of the human skull: results of in-vivo and in-vitro measurements. IEEE Trans Biomed Eng 2000];47(11):1487–92.
Gonçalves S, de Munck JC, Verbunt JP, Bijma F, Heethaar RM, da Silva FL. In vivo measurement of the brain and skull resistivities using an EIT-based method and realistic models for the head. IEEE Trans Biomed Eng 2003];50(6):754–67.
Gutierrez D, Nehorai A, Muravchik CH. Estimating brain conductivities and dipole source signals with EEG arrays. IEEE Trans Biomed Eng 2004];51(12):2113–22.
Lai Y, Drongelen W, Ding L, Hecox KE, Towle VL, Frim DM, He B. Estimation of in vivo human brain-to-skull conductivity ratio from simultaneous extra- and intracranial electrical potential recordings. Clin Neurophysiol 2005];116:456–65.
Zhang Y, van Drongelen W, He B. Estimation of in vivo brain-to-skull conductivity ratio in humans. Appl Phys Lett 2006];89:2239031–3.
Ryynänen O, Hyttinen J, Malmivuo J. Effect of measurement noise and electrode density on the spatial resolution of cortical potential distribution with different resistivity values for the skull. IEEE Trans Biomed Eng 2006];53(9):1851–8.
Wang G, Ren D. Effect of brain-to-skull conductivity ratio on EEG source localization accuracy. BioMed Res Int 2013];2013:459346.
Huiskamp G, Vroeijenstijn M, van Dijk R, Wieneke G, van Huffelen AC. The need for correct realistic geometry in the inverse EEG problem. IEEE Trans Biomed Eng 1999];46:1281–7.
Song J, Morgan K, Sergei T, Li K, Davey C, Govyadinov P, Luu P, Smith K, Prior F, Larson-Prior L, Tucker D. Anatomically accurate head models and their derivatives

for dense array EEG source localization, functional neurology. Rehabil Ergon 2013];3(2):275–94.
Freeman WJ, Holmes M, Burke B, Vanhatalo S. Spatial spectra of scalp EEG and EMG from awake humans. Clin Neurophysiol 2003];114(6):1053–68.
Odabaee M, Freeman W, Colditz P, Ramon C, Vanhatalo S. Spatial patterning of the neonatal EEG suggests a need for a high number of electrodes. Neuroimage 2013];68:229–35.
Malmivuo J, Suihko V, Eskola H. Sensitivity distributions of EEG and MEG measurements. IEEE Trans Biomed Eng 1997];44(3):196–208.
Malmivuo JA, Suihko VE. Effect of skull resistivity on the spatial resolutions of EEG and MEG. IEEE Trans Biomed Eng 2004];51(7):1276–80.
Ryynänen O, Hyttinen J, Laarne P, Malmivuo J. Effect of electrode density and measurement noise on the spatial resolution of cortical potential distribution. IEEE Trans Biomed Eng 2004];51(9):1547–54.
Luu P, Tucker DM, Englander R, Lockfeld A, Lutsep H, Oken B. Localizing acute stroke-related EEG changes: assessing the effects of spatial undersampling. J Clin Neurophysiol 2001];18(4):302–17.
Sperli F, Spinelli L, Seeck M, Kurian M, Michel C, Lantz G. EEG source imaging in pediatric epilepsy surgery: a new perspective in presurgical workup. Epilepsia 2006];47(6):981–90.
Fitzgibbon S, Lewis T, Powers D, Whitham E, Willoughby J, Pope K. Surface laplacian of central scalp electrical signals is insensitive to muscle contamination. IEEE Trans Biomed Eng 2013];60(2):4–9.
Moretti DV, Babiloni F, Carducci F, Cincotti F, Remondini E, Rossini PM, Salinari S, Babiloni C. Computerized processing of EEG-EOG-EMG artifacts for multi-centric studies in EEG oscillations and event-related potentials. Int J Psychophysiol 2003];47(3):199–216.
Gao J, Yang Y, Sun J, Yu G. Automatic removal of various artifacts from EEG signals using combined methods. J Clin Neurophysiol 2010];27(5):312–20.
Shackman AJ, McMenamin BW, Slagter HA, Maxwell JS, Greischar LL, Davidson RJ. Electromyogenic artifacts and electroencephalographic inferences. Brain Topogr 2009];22:7–12.
McMenamin BW, Shackman AJ, Greischar LL, Davidson RJ. Electromyogenic artifacts and electroencephalographic inferences revisited. Neuroimage 2011];54:4–9.
Olbrich S, Jodicke J, Sander C, Himmerich H, Hegerl U. ICA-based muscle artefact correction of EEG data: what is muscle and what is brain? Comment on McMenamin et al. Neuroimage 2011];54:1–3.
Gross J, Baillet S, Barnes GR, Henson RN, Hillebrand A, Jensen O, Jerbi K, Litvak V, Maess B, Oostenveld R, Parkkonen L, Taylor J, van Wassenhove V, Wibral M, Schoffelen JM. Good-practice for conducting and reporting MEG research. Neuroimage 2013];65:349–63.
Pascual-Marqui R. Standardized low resolution brain electromagnetic tomography (sLORETA): technical details. Methods Find Clin Pharmacol 2002];24D:5–12.
Mosher JC, Leahy RM, Lewis PS. EEG and MEG. Forward solutions for inverse methods. IEEE Trans Biomed Eng 1999];46(3):245–59.
Berg P, Scherg M. A fast method for forward computation of multiple-shell spherical head models. Electroencephalogr Clin Neurophysiol 1994];90:58–64.
Zhang Z. A fast method to compute surface potentials generated by dipoles within multilayer anisotropic spheres. Phys Med Biol 1995];40:335–49.
Hallez H, Vanrumste B, Grech R, Muscat J, Clercq WD, Vergult A, D'Asseler Y, Camilleri KP, Fabri SG, Huffel SV, Lemahieu I. Review on solving the forward problem in EEG source analysis. J NeuroEng Rehabil 2007];4:46.
He B, Yao D, Lian J. High-resolution EEG: on the cortical equivalent dipole layer imaging. Clin Neurophysiol 2002];113:227–35.
Ary JP, Klein S, Fender DH. Location of sources of evoked scalp potentials: corrections for skull and scalp thicknesses. IEEE Trans Biomed Eng 1981];28(6):447–52.
Fuchs M, Drenckhahn R, Wischmann HA, Wagner MM. An improved boundary element method for realistic volume-conductor modeling. IEEE Trans Biomed Eng 1998];45(8):980–97.
Pascual-Marqui RD, Michel CM, Lehmann D. Low-resolution electromagnetic tomography: a new method for localizing activity in the brain. Int J Psychophysiol 1994];18:49–65.
Russell GS, Eriksen KJ, Poolman P, Luu P, Tucker DM. Geodesic photogrammetry for localizing sensor positions in dense array EEG. Clin Neurophysiol 2005];116(5):1130–40.
D. M. Tucker, S. E. Tucker, Method for mapping internal body tissue, US Patent 6,529,759 (March 2003), http://www.google.com/patents/US6529759
Li K, Malony A, Tucker DM. Automatic brain MR image segmentation by relative thresholding and morphological image analysis. In: First International Conference on Computer Vision Theory and Applications (VISAPP); February 2006. p. 354–64.
K. Li, A. D. Malony, D. M. Tucker, Image segmentation method, US Patent App.12/587,225 (April 2011), http://www.google.com/patents/US20110081062
Malony A, Salman A, Turovets S, Tucker D, Volkov V, Li K, Song J, Biersdorff S, Davey C, Hodge C, Hammond D. Computational Modeling of Human Head Electromagnetics for Source Localization of Milliscale Brain Dynamics. In: Proceedings of Medicine Meets Virtual Reality (MMVR); 2011].
Smith K, Politte D, Reiker G, Nolan T, Hildebolt C, Mattson C, Tucker D, Prior F, Turovets S, Larson-Prior L. Automated measurement of pediatric cranial bone thickness and density from clinical computed tomography. In: Conf Proc IEEE Eng Med Biol Soc; 2012]. p. 4462–5, http://dx.doi.org/10.1109/EMBC.2012.6346957.
Ferree T, Eriksen KJ, Tucker DM. Region head tissue conductivity estimation for improved EEG analysis. IEEE Trans Biomed Eng 2000];47:1584–92.
Rush S, Driscoll D. EEG-electrode sensitivity: an application reciprocity. IEEE Trans Biomed Eng 1969];16(1):15.
Salman A, Turovets S, Malony A, Volkov V. Multi-cluster mix-mode computational modeling of human head conductivity. International Workshop on OpenMP (IWOMP 2005/2006) LNCS 4315; 2008]. p. 119–30.
Turovets S, Poolman P, Salman A, Malony A, Tucker D. Conductivity analysis for high-resolution EEG. In: IEEE Computer Society International Conference on Biomedical Engineering and Informatics; 2008]. p. 386–93.
Ida N. Engineering electromagnetics. 3rd ed. Springer; 2015].
Jin JM. The finite element method in electromagnetics. 2nd ed. New York: John Wiley & Sons; 2002].
Gaul L, Kögl M, Wagner M. Boundary element methods for engineers and scientists: an introductory course with advanced topics. Berlin, Heidelberg: Springer; 2012] https://books.google.com/books?id=7ZR2cgAACAAJ
Salman A, Malony A, Turovets S, Volkov V, Ozog D, Tucker DM. Concurrency in electrical neuroinformatics: parallel computation for studying the volume conduction of brain electrical fields in human head tissues. Concurr Comput Pract Exp 2015].
Grech R, Cassar T, Muscat J, Camilleri KP, Fabri SG, Zervakis M, Xanthopoulos P, Sakkalis V, Vanrumste B. Review on solving the inverse problem in EEG source analysis. J NeuroEng Rehabil 2008];5:25.
Baillet S, Mosher JC, Leahy RM. Electromagnetic brain mapping. IEEE Signal Process Mag 2001];18:14–30.
Yao J, Dewald JPA. Evaluation of different cortical source localization methods using simulated and experimental EEG data. NeuroImage 2005];25:369–82.
Fuchs M, Wagner M, Wischmann HA, Köhler T, Theissen A, Drenckhahn R, Buchner H. Improving source reconstructions by combining bioelectric and biomagnetic data. Electroencephalogr Clin Neurophysiol 1998];107(2):93–111.
Mosher JC, Leahy RM, Recursive. MUSIC: a framework for EEG and MEG source localization. IEEE Trans Biomed Eng 1998];45(11):1342–54.
Mosher JC, Leahy RM. Source localization using recursively applied and projected (RAP) MUSIC. IEEE Trans Biomed Eng 1999];47:332–40.
Veen BDV, van Drongelen W, Yuchtman M, Suzuki A. Localization of brain electrical activity via linearly constrained minimum variance spatial filtering. IEEE Trans Biomed Eng 1997];44(9):867–80.
de Peralta-Menendez RG, Murray MM, Michel CM, Martuzzi R, Gonzalez-Andino SL. Electrical neuroimaging based on biophysical constraints. NeuroImage 2004];21:527–39.
Michel CM, Murray MM, Lantz G, Gonzalez S, Spinelli L, de Peralta RG. EEG source imaging. Clin Neurophysiol 2004];115:2195–222.
Abascal JFPJ, Arridge SR, Bayford RH, Holder DS. Comparison of methods for optimal choice of the regularization parameter for linear electrical impedance tomography of brain function. Physiol Meas 2008];29(11):1319, http://dx.doi.org/10.1088/0967-3334/29/11/007.
Hauk O, Wakeman D, Henson R. Comparison of noise-normalized minimum norm estimates for MEG analysis using multiple resolution metrics. Neuroimage 2010];54:1966–74, http://dx.doi.org/10.1016/j.neuroimage.2010.09.053.
Engel J. Surgical treatment of the epilepsies. 2nd ed. Lippincott Williams & Wilkins; 1993].
Lehmann D, Skrandies W. Reference-free identification of components of checkerboard-evoked multichannel potential fields. Electroencephalogr Clin Neurophysiol 1980];48:609–21.
Laarne PH, Tenhunen-Eskelinen ML, Hyttinen J, Eskola HJ. Effect of EEG electrode density on dipole localization accuracy using two realistically shaped skull resistivity models. Brain Topogr 2000];12:249–54.
Nunez P, Srinivasan R. Electric fields of the brain: the neurophysics of EEG. 2nd ed. New York, Oxford: Oxford University Press; 2005].
Song J, Davey C, Poulsen C, Sergei T, Luu P, Tucker D. Sensor density and head surface coverage in EEG source localization. Beijing, China: ISBI; 2014].
Sohrabpour A, Lu Y, Kankirawatana P, Blount J, Kim H, He B. Effect of EEG electrode number on epileptic source localization in pediatric patients. Clin Neurophysiol 2015];126(3):472–80.
Oostenveld R, Praamstra P. The five percent electrode system for high-resolution EEG and ERP measurements. Clin Neurophysiol 2001];112:713–9.
Feng R, Hu J, Pan L, Wu J, Lang L, Jiang S, Guo XGJ, Zhou L. Application of 256-channel dense array electroencephalographic source imaging in presurgical workup of temporal lobe epilepsy. Clin Neurophysiol 2015].
Perrin F, Bertrand O, Giard MH, Pernier J. Precautions in topographic mapping and in evoked potential map reading. J Clin Neurophysiol 1990];7(4):498–506.
Yvert B, Bertrand O, Thevenet M, Echallier J, Pernier J. A systematic evaluation of the spherical model accuracy in EEG dipole localization. Electroencephologr Clin Neurophysiol 1997];102:452–9.
Wipf DP, Owen JP, Attias HT, Nagarajan KSSS. Robust Bayesian estimation of the location, orientation, and time course of multiple correlated neural sources using MEG. Neuroimage 2010];49:641–55.